Contract No:

This document was prepared in conjunction with work accomplished under Contract No. DE-AC09-08SR22470 with the U.S. Department of Energy (DOE) Office of Environmental Management (EM).

Disclaimer:

This work was prepared under an agreement with and funded by the U.S. Government. Neither the U. S. Government or its employees, nor any of its contractors, subcontractors or their employees, makes any express or implied:

   1) warranty or assumes any legal liability for the accuracy, completeness, or for the use or results of such use of any information, product, or process disclosed; or
   2) representation that such use or results of such use would not infringe privately owned rights; or
   3) endorsement or recommendation of any specifically identified commercial product, process, or service.

Any views and opinions of authors expressed in this work do not necessarily state or reflect those of the United States Government, or its contractors, or subcontractors.

PVP2018-84919

MODELING OF CRACK EXTENSIONS IN ARC-SHAPED SPECIMENS OF HYDROGEN-CHARGED AUSTENITIC STAINLESS STEELS USING COHESIVE ZONE MODEL

Shengjia Wu, Shin-Jang Sung, Jwo Pan
Department of Mechanical Engineering
University of Michigan
Ann Arbor, Michigan, USA

Poh-Sang Lam, Michael J. Morgan, Paul S. Korinko
Materials Science and Technology
Savannah River National Laboratory
Aiken, South Carolina, USA

ABSTRACT

Crack extensions in arc-shaped specimens of hydrogen-charged and as-received conventionally forged (CF) 21-6-9 austenitic stainless steels are investigated by two-dimensional finite element analyses with the cohesive zone model. The material constitutive relation is first obtained from fitting the experimental tensile stress-strain data by conducting an axisymmetric finite element analysis of a round bar tensile specimen of the as-received CF steel. The material constitutive relation for the hydrogen-charged CF steel is estimated based on the experimental tensile stress-strain data of the as-received CF steel and the hydrogen-charged high-energy-rate-forged (HERF) 21-6-9 stainless steel. The cohesive zone model with the exponential traction-separation law is then adopted to simulate crack extensions in arc-shaped specimens of the hydrogen-charged and as-received CF steels. The cohesive strength of the cohesive zone model is calibrated to match the experimental load-displacement curve with the cohesive energy determined by the J-integral at the maximum load of the arc-shaped specimen. The computational results showed that the numerical predictions of the load-displacement and crack extension-displacement curves for the hydrogen-charged and as-received CF steel specimens are compared reasonably well with the experimental data.

1. INTRODUCTION

Austenitic stainless steels are used to fabricate containment vessels for hydrogen and its isotopes because of their high resistance to hydrogen-induced embrittlement [1,2]. However, the structural properties may still degrade during the long service life as the hydrogen atoms diffuse into the vessel walls and make the vessels susceptible to cracking. The degree of embrittlement is exacerbated in the presence of helium-3 (^{3}He), which is the byproduct from the radioactive decay of a hydrogen isotope (^{3}H). Typically, steels with decay helium bubbles embedded in the microstructure are hardened and less able to deform plastically. Uniaxial tension tests were conducted to obtain the stress-strain curves of high-energy-rate-forged (HERF) 21-6-9 stainless steels [1] and fracture tests were conducted to obtain the crack growth resistance J-integral curves (J-R curves) of conventionally forged (CF) 21-6-9 stainless steels and high-energy-rate-forged (HERF) 21-6-9 stainless steels [2]. However, the test data have not been analyzed to develop predictive fracture mechanics models to reduce the time and resources for evaluating the material performance of these steels.

In this paper, the fracture test data of the hydrogen-charged and as-received CF 21-6-9 austenitic stainless steels are analyzed to examine the predictability of the cohesive zone model [3-8] for the experimental load-displacement-crack extension data. The material constitutive relation is first obtained from fitting the experimental tensile stress-strain data by conducting an axisymmetric finite element analysis of a round bar tensile specimen of the as-received CF steel. The material constitutive relation for the hydrogen-charged CF steel is estimated based on the experimental tensile stress-strain data of the as-received CF steel and the hydrogen-charged high-energy-rate-forged (HERF) 21-6-9 stainless steel. The cohesive zone model with the exponential traction-separation law is then adopted to simulate crack extensions in arc-shaped specimens of the hydrogen-charged and as-received CF steels. The cohesive strength of the cohesive zone model is calibrated to match the experimental load-displacement curve with the cohesive energy determined by the J-integral at the maximum load of the arc-shaped specimen. The numerical predictions of the load-displacement, load-crack extension and crack

extension-displacement curves for the hydrogen-charged and as-received CF steel specimens are then compared with the experimental data. Finally, conclusions are made.

2. UNIAXIAL TENSION TEST

Standard round bar tensile specimens of CF 21-6-9 stainless steel were tested and reported in [1]. Figure 1(a) shows a finite element model of the axisymmetric round bar specimen used in the tensile test. The test specimen (Specimen No. CF H94 #2, as-received or uncharged) analyzed in the present work has a radius R of 1.6129 mm and a gauge length L of 15.875 mm. Due to the symmetry, only the upper part of the tensile specimen is modeled as shown in Figure 1(a). The coordinate system is also shown in Figure 1(a). The boundary condition of the y-symmetry is placed on the mid-section of the specimen and a uniform displacement is applied at the upper surface in the y direction. The finite element model has the same dimensions as the experimental tensile test specimens except the geometry imperfection of $\Delta R = 0.0004$ mm introduced in the mid-section of the specimen at y= 0 to trigger necking. The ABAQUS four-node bilinear axisymmetric elements (CAX4) were used in the finite element analysis. Figure 1(b) shows the finite element mesh. The element size near the upper surface is 0.08×0.05 mm and near the mid-section is 0.078×0.005 mm. The total number of elements is 8,000.
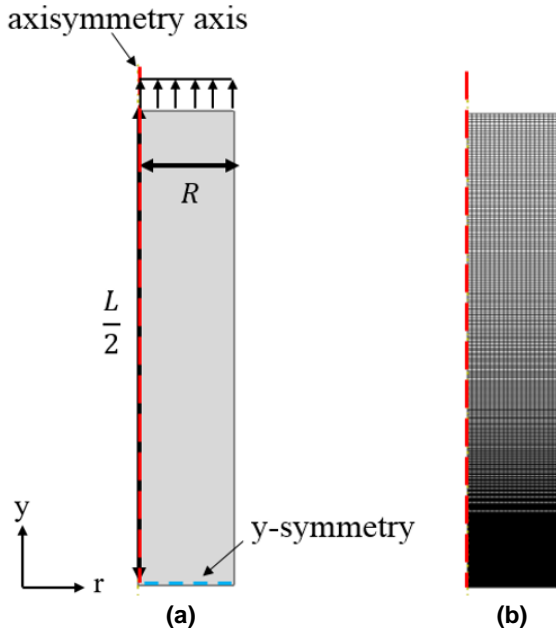

Figure 1. (a) The finite element model and the boundary conditions and (b) the mesh of the tensile specimen.

Figure 2(a) shows the engineering stress-engineering strain curve as the black solid curve for the as-received CF steel [1]. An elastic-plastic stress-strain relation is used to fit the experimental tensile stress-strain curve for the as-received CF steel in the finite element analysis. When the stress σ is less

than the yield stress σ_Y, the stress σ is related to the strain ε by the Young's modulus E as

$$\sigma = E\varepsilon, \qquad \sigma < \sigma_Y \tag{1}$$

When the stress σ is larger than the yield stress σ_Y, the true stress-true plastic strain curve is used up to the true plastic strain ε_p equal to 0.246 corresponding to the tensile strength from the experiment [1]. When the true stress σ is larger than the true stress σ_U corresponding to the tensile strength, a power law is used for the curve of the true stress σ and the true plastic strain ε_p as

$$\sigma = K\varepsilon_p^n, \qquad \sigma > \sigma_U \tag{2}$$

Here, K is a material constant and n is the strain hardening exponent. The material constant K and the hardening exponent n are determined by fitting to the experimental data up to the true stress σ_U corresponding to the tensile strength. Figure 2(b) shows the true stress-true plastic strain curve as a black solid line for $\sigma_Y = 856.48$ MPa, $K = 1,770$ MPa, and $n = 0.225$. For the finite element analysis of the tensile test of the as-received CF steel, $E = 177.33$ GPa and the Poisson's ratio $\nu = 0.3$ are used for the elastic response. The material constants for the as-received CF steel are listed in Table 1. Figure 2(a) shows a comparison of the tensile responses of the experimental results as a black solid line and the computational results as a red solid line with circles based on the stress-strain relation as discussed earlier as the input to the ABAQUS finite element analysis. The good agreement confirms that the stress-strain relation as discussed earlier is a reasonable constitutive relation. The deformed mesh of the specimen with the necking near the mid-section of the specimen at the displacement of 3 mm in the y direction on the upper surface is shown in Figure 2(c).

The tensile stress-strain curve for the hydrogen-charged CF steel with the hydrogen concentration of 78 wppm, which matches that of the hydrogen-charged arc-shaped CF steel specimen, is not available. Therefore, an estimation procedure was used to estimate the stress-strain curve for the hydrogen-charged CF steel based on the yield stresses of the high-energy-rate-forged (HERF) steels [2]. The interpolation was carried out in terms of the hydrogen concentration of the HERF steels with respect to the yield stress to obtain the plastic response of the hydrogen-charged CF steel. The interpolation procedure is summarized in Table 2. Here, two groups of uncharged HERF steels and hydrogen-charged HERF steels with the hydrogen concentration of 210 wppm as reported in [2] were selected as the reference steels for the interpolation procedure. The uncharged steel A and the hydrogen-charged steel A have the low yield stresses of 825 MPa and 836 MPa, respectively. The uncharged steel B and the hydrogen-charged steel B have the high yield stresses of 918 MPa and 965 MPa, respectively. Based on the hydrogen concentration, the linearly interpolated yield stresses of the hydrogen-charged A and B steels with the hydrogen concentration of 78 wppm are 829 MPa and 935

MPa, respectively. For the target uncharged steel with the yield stress of 856 MPa and for the target hydrogen-charged steel with the hydrogen concentration of 78 wppm, the linearly interpolated yield stress of the target hydrogen-charged steel is 867 MPa.

With the assumption that the effects of the hydrogen concentration on the increase of the yield stress for both the CF and HERF steels are similar, the yield stress for the hydrogen-charged CF steel with the hydrogen concentration of 78 wppm is assumed to be 867 MPa of the target HERF steel. The true stress-true plastic strain of the hydrogen-charged CF steel is then scaled up from the uncharged one by the larger yield stress of 867 MPa. The resulting tensile properties with $\sigma_Y = 867.53$ MPa, $K = 1,793$ MPa, and $n = 0.225$ for the hydrogen-charged CF steel with the hydrogen concentration of 78 wppm are listed in Table 1. Due to the small effects of the hydrogen concentration, the estimated tensile true stress-true plastic strain curve as the dashed line for the hydrogen-charged CF steel is about 1.3% higher than the uncharged one as the solid line in Figure 2(b). For the finite element simulation of the crack extension in the arc-shaped specimen of the hydrogen-charged CF steel, the estimated true stress-true plastic strain curve for the hydrogen-changed CF steel shown in Figure 2(b) will be used.
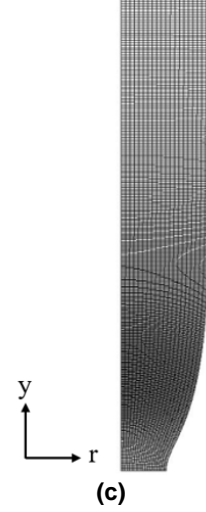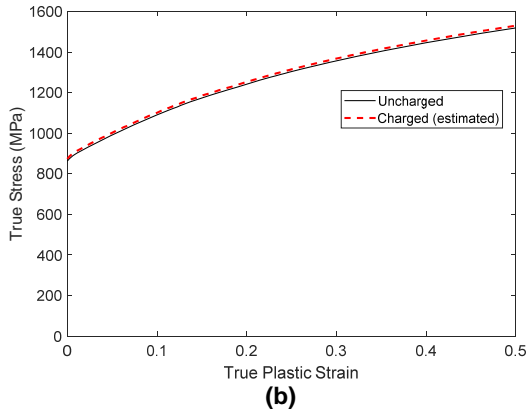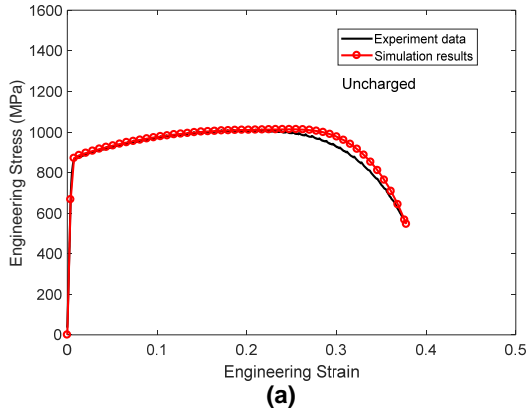

(c)

Figure 2: (a) The experimental data and simulation results of the uniaxial tension test of the uncharged CF steel, (b) the true stress-true plastic strain curves for the uncharged and hydrogen-charged CF steels, and (c) the deformed shape of the finite element mesh for the uncharged steel at the displacement of 3 mm.

**Table 1. The material constants for the as-received and hydrogen-charged CF 21-6-9 steels**

Specimen	E (GPa)	ν	σ_Y (MPa)	K (MPa)	n
As-received	177.33	0.3	856.48	1,770	0.225
Hydrogen-charged	177.33	0.3	867.53	1,793	0.225

Table 2. Experimental and interpolated yield stresses for the uncharged and hydrogen-charged HERF steels.

Steel	Yield stress (MPa) from experiment for hydrogen concentration of 0 wppm	Yield stress (MPa) from interpolation for hydrogen concentration of 78 wppm	Yield stress (MPa) from experiment for hydrogen concentration of 210 wppm
A	825	829 (interpolated)	836
Target	856	867 (estimated)	
B	918	935 (interpolated)	965

(a)

(b)

3. FRACTURE TESTS

Arc-shaped fracture mechanics specimens were made and tested [2]. An arc-shaped fracture mechanics specimen is schematically shown in Figure 3. The specimens were fatigue-cracked before the fracture tests. The crack lengths with consideration of the fatigue pre-crack lengths are 5.75 mm for the as-received CF steel specimen and 4.82 mm for the hydrogen-charged CF steel specimen, respectively. The hydrogen-charged arc-shaped specimens were prepared by exposing the pre-cracked specimens to hydrogen gas at 34.47 MPa at 350 °C for three weeks. The hydrogen concentration of the specimen was measured to be 78 wppm as mentioned earlier. Both the uncharged (as-received) and hydrogen-charged arc-shaped specimens were tested.

3
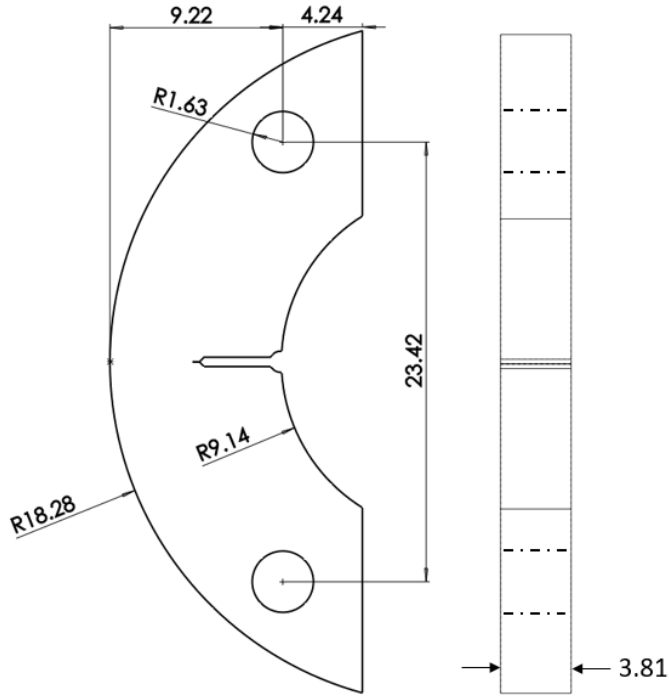
Note: All dimensions are in mm

Figure 3. A schematic of an arc-shaped specimen.

The J-integral fracture tests [2] were conducted at room temperature in air using a screw-driven testing machine with a crosshead speed of 0.002 mm/s. The load, load-line displacement (using a gage clipped to the crack mouth), and crack length were recorded during the tests. The crack length was monitored using an alternating direct current potential drop system following the guidelines provided in ASTM E647 [9]. The J-integral vs. crack extension (J vs. Δa) curves were constructed from the data using ASTM E1820 [10]. The J-R curves for the arc-shaped specimens of the uncharged (Specimen No. H94-2) and the hydrogen-charged (Specimen No. H94-54) CF 21-6-9 steels are shown in Figure 4. The values of the crack extension and J-integral at the maximum loads are (0.269 mm, 273.1 kJ/m^2) and (0.175 mm, 180.3 kJ/m^2), respectively, and are marked in Figure 4 for the uncharged and hydrogen-charged specimens. It should be noted that the stress-strain curve for the uncharged CF steel and the estimated stress-strain curve for the hydrogen-charged CF steel are very close as shown in Figure 2(b), but their J-R curves obtained from the arc-shaped specimens are significantly different as shown in Figure 4.
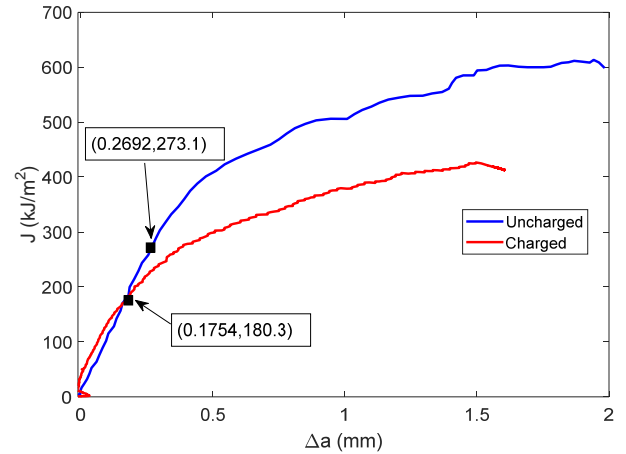

Figure 4. The J-integral vs. crack extension (J-R) curves for the uncharged and hydrogen-charged CF steel specimens. The Δa and J values at the maximum loads are identified on the curves.

4. TWO-DIMENSIONAL (2-D) PLANE STRAIN MODELING OF FRACTURE TESTS

4.1 Finite Element Model

The geometry of the 2-D finite element models follows the geometry of the arc-shaped specimen shown in Figure 3. The crack lengths including the fatigue pre-crack lengths are 5.75 mm and 4.82 mm, respectively, for the uncharged specimen (Specimen No. H94-2) and the hydrogen-charged specimen (Specimen No. H94-54). The specimen thickness is 4.6 mm for the as-received and hydrogen-charged specimens. The net section thickness is 3.8 mm without counting side grooves. The true stress-true plastic strain curves for the uncharged steel (solid line) and the hydrogen-charged steel (dashed line) shown in Figure 2(b) are used in the fracture test simulations.

Figure 5(a) shows the 2-D finite element model of the arc-shaped specimen of the hydrogen-charged steel in a Cartesian $X - Y$ coordinate system, and Figure 5(b) shows a closeup view near the crack tip. The model contains four regions with different mesh sizes. Region 1 is far away from the crack and has the coarsest mesh, while Region 4 is closest to the crack line and has the finest mesh. The mesh sizes for Regions 1 to 4 are listed in Table 3. Tie constraints are used between the regions. The 2-D finite element model of the arc-shaped specimen of the as-received steel is quite similar and will not be shown. Plane strain linear elements with full integration (CPE4) are used to model the arc-shaped specimen. The PPR user-defined cohesive element subroutine [11,12] for ABAQUS is adopted here but with the exponential traction-separation law. Note that the ABAQUS built-in cohesive elements are not used in this analysis. The cohesive elements are placed along the crack line ahead of the crack tip in the -X direction. All cohesive elements have the same element size of 0.005 mm, and the total numbers of cohesive elements are 679 and 864,

respectively, for the arc-shaped specimens of the as-received and the hydrogen-charged steels.
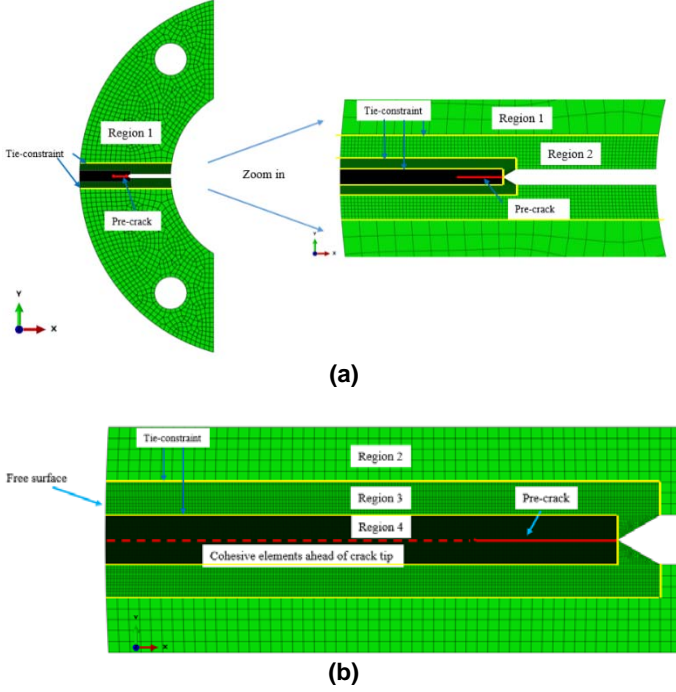

(a)

(b)

Figure 5. (a) The finite element model of the arc-shaped specimen of the hydrogen-charged steel and (b) a closeup view of the refined mesh near the crack tip with the cohesive elements along the crack line. Tie constraints are used between the regions.

Table 3. Finite element regions and mesh sizes for the plane strain model of the arc-shaped specimen of the hydrogen-charged steel

Region	Element size	Number of elements
1	500×500 µm	1,284
2	100×100 µm	1,534
3	20×20 µm	7,958
4	5×5 µm	86,480

4.2 Cohesive Zone Model

Trapezoidal [3,4,7,8] or exponential [5,6] traction-separation laws were used to characterize the crack extensions in ductile metals. Tvergaard and Hutchinson [3] indicated that the shape of the traction-separation law on the fracture behavior is not significant. Thus, by considering the computational efficiency and avoiding convergence problems, the exponential traction-separation law is selected for the present preliminary study.

Figure 6 schematically shows the normalized exponential traction-separation law used in this study. The traction σ is normalized by the cohesive strength σ_{max} which is the maximum traction that can be sustained in the cohesive zone model. The separation δ is normalized by the critical separation

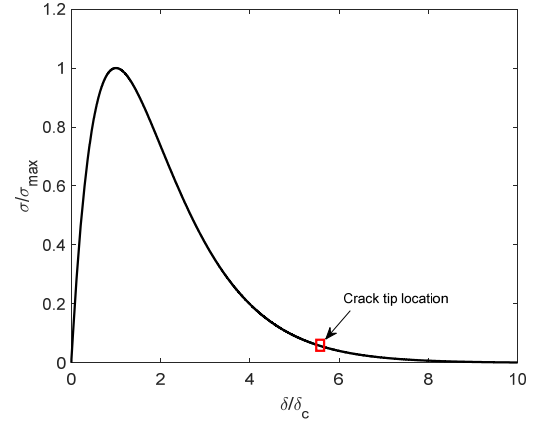δ_c which is the separation corresponding to the cohesive strength σ_{max}.

Figure 6. A normalized exponential traction-separation law. The crack tip is commonly selected at the location where the traction σ is dropped to 5% of σ_{max}.

The exponential traction-separation law is expressed as

$$\sigma = e\sigma_{max}\frac{\delta}{\delta_c}e^{-\frac{\delta}{\delta_c}} \qquad (3)$$

The cohesive energy Γ commonly used in the cohesive zone modeling is represented by the area under the traction-separation curve. Equation (3) is integrated to obtain a closed form cohesive energy Γ as

$$\Gamma = e\sigma_{max}\delta_c \qquad (4)$$

In this study, the cohesive strength σ_{max} and the cohesive energy Γ are used to define the exponential traction-separation law. The crack tip is selected at the location where the traction σ drops to 5% of σ_{max}.

4.3 Selection of cohesive parameters

Besides the shape of the traction-separation law, the cohesive strength σ_{max} and the cohesive energy Γ are the two major cohesive parameters for the cohesive zone model. In the current exploratory study using the exponential traction-separation law, the cohesive energy Γ is selected as $\Gamma = J_{max}$, where J_{max} is the J-integral at the maximum load from the test data of the arc-shaped specimen of the hydrogen-charged steel. The experimental data of the maximum load, crack extension Δa at the maximum load, and J_{max} are listed in Table 4 for the hydrogen-charged steel specimen. The cohesive strength σ_{max} is selected as $\sigma_{max} = 2.45\sigma_Y$ to best fit the maximum load of the load vs. displacement curve for the hydrogen-charged steel. The cohesive strength σ_{max}, the cohesive energy Γ, and the

critical separation δ_c for the hydrogen-charged steel specimen are listed in Table 5.

For the as-received steel specimen, the cohesive strength σ_{max} is taken as the same as the cohesive strength of the hydrogen-charged steel specimen. However, the cohesive energy Γ is selected as the J_{max} for the arc-shaped specimen of the as-received steel. The experimental data of the maximum load, crack extension Δa at the maximum load, and J_{max} are also listed in Table 4 for the as-received steel. The cohesive strength σ_{max}, the cohesive energy Γ, and the critical separation δ_c for the as-received steel specimen are also listed in Table 5. Figure 7 shows the exponential traction–separation laws for both the uncharged and the hydrogen-charged steels. Note that the hydrogen-charged steel has the narrower shape of the exponential traction-separation curve because of the smaller cohesive energy Γ, as compared with the wider one of the uncharged steel.

Table 4. Experimental data corresponding to the maximum loads of fracture tests.

Specimen	Maximum load (N)	Δa (mm)	J_{max} (kJ/m^2)
Uncharged	2,037	0.2692	273.1
Hydrogen-charged	3,717	0.1754	180.3

Table 5. The cohesive parameters for the exponential traction-separation law.

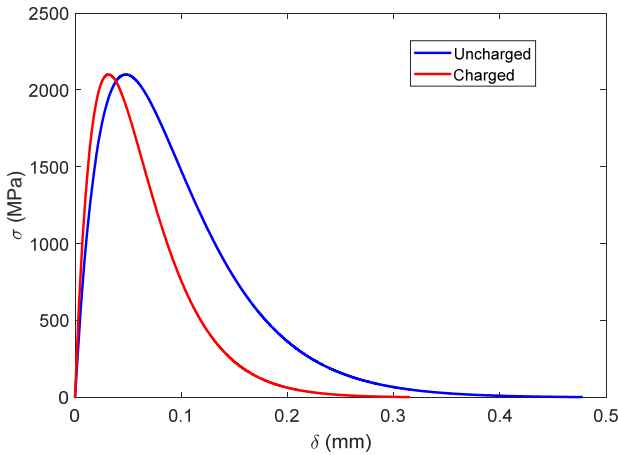| Specimen	σ_{max} (MPa)	Γ (kJ/m^2)	δ_c (µm)
Uncharged	2,100	273.1	47.80
Hydrogen-charged	2,100	180.3	30.15

Figure 7. The exponential traction-separation laws for the uncharged and hydrogen-charged CF 21-6-9 austenitic stainless steels.

4.4 Computational Results

The experimental and predicted load vs. displacement, load vs. crack extension Δa, and crack extension Δa vs. displacement curves for the charged specimen are shown in Figures 8(a) to 8(c). Because the cohesive strength $\sigma_{max} = 2.45\sigma_Y$ is selected to fit the maximum load of the load vs. displacement data, the predicted curve shown in Figure 8(a) is in good agreement with the experimental data. The crack tip location at crack initiation defined by the traction of the finite element ahead of the crack tip decreasing to 5% of σ_{max} is also labelled on the predicted curve shown as the red dashed curve. However, the predicted load vs. Δa curve in Figure 8(b) has noticeable discrepancy from the experimental data. However, the predicted Δa vs. displacement curve is in good agreement with the experimental data as shown in Figure 8(c).
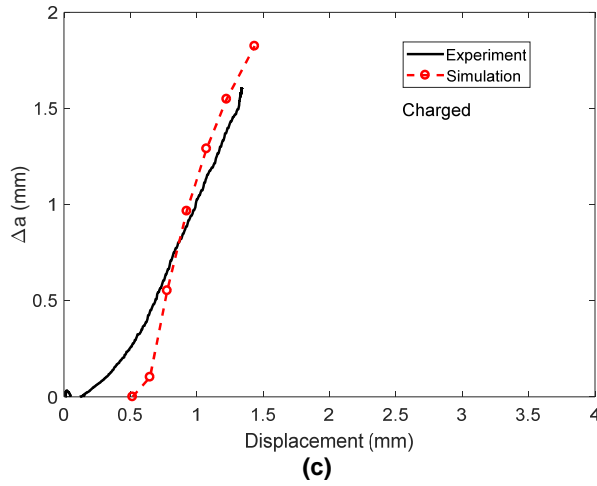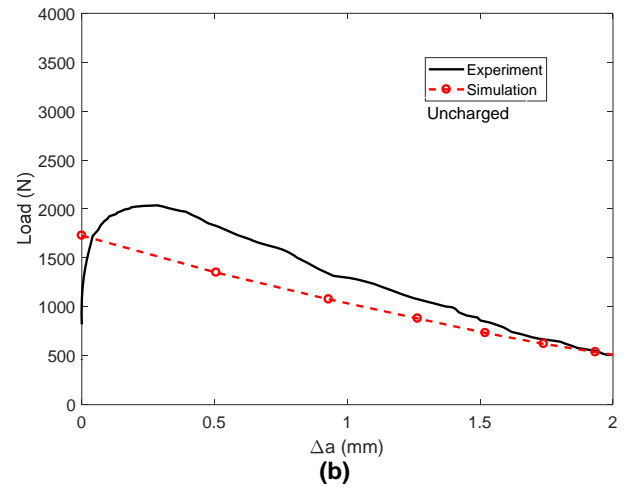

(a)

(b)

(c)
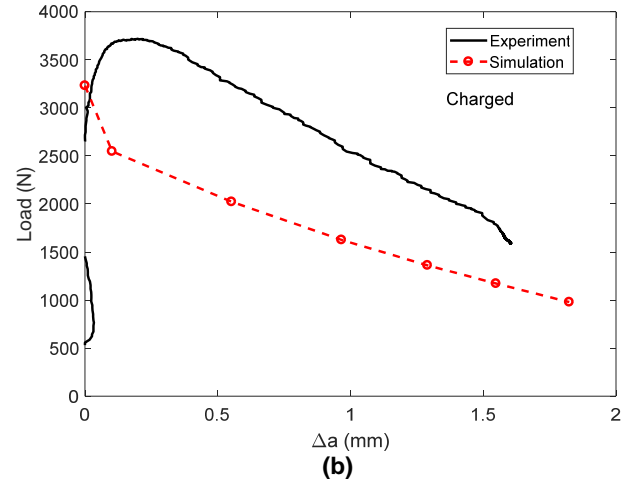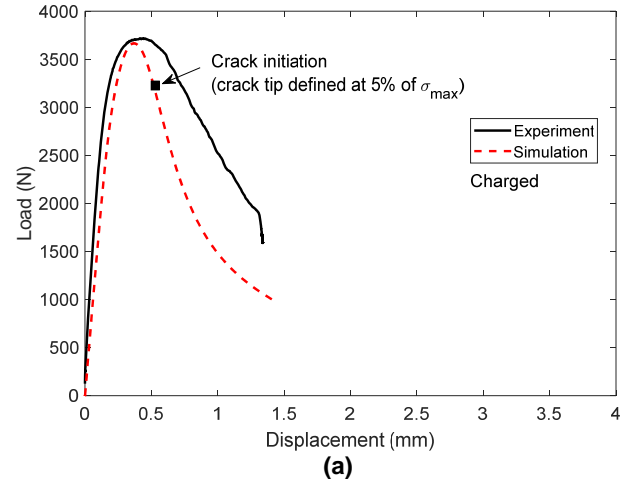
Figure 8. Comparisons of the experimental and numerical results for the hydrogen-charged steel specimen: (a) load vs. displacement curves, (b) load vs. crack extension curves, and (c) crack extension vs. displacement curves.

For the as-received steel, the experimental and predicted load vs. displacement, load vs. Δa, and Δa vs. displacement curves are shown in Figures 9(a) to 9(c). The predicted load vs. displacement curve in Figure 9(a) agrees reasonably well with the experimental curve with the cohesive strength $\sigma_{max} = 2.45\sigma_Y$ being selected to fit the maximum load of the load vs. displacement test data of the hydrogen-charged specimen. The predicted load vs. Δa and Δa vs. displacement curves shown in Figures 9(b) and 9(c) are also in good agreement with the experimental data.
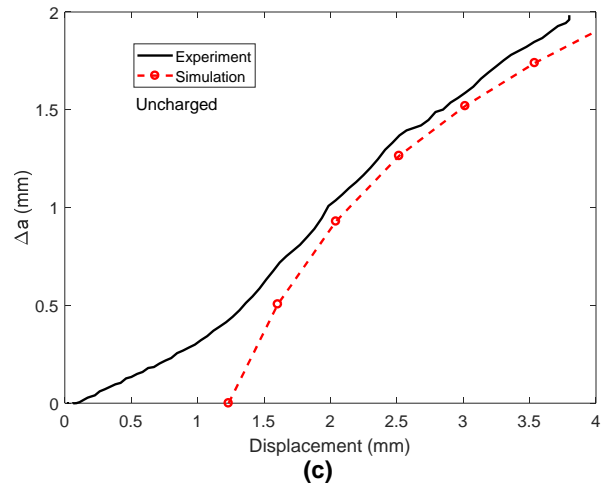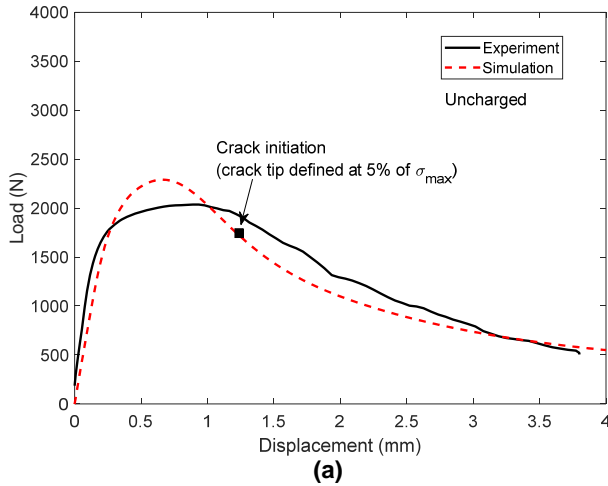

(a)

(b)

(c)

Figure 9. Comparisons of the experimental and numerical results for the uncharged steel: (a) load vs. displacement curves, (b) load vs. crack extension curves, and (c) crack extension vs. displacement curves.

5. CONCLUSIONS

Austenitic stainless steels have been used to fabricate hydrogen and hydrogen isotope containment vessels. It is well known that the hydrogen permeation into the steels would cause material embrittlement and ductility loss. The decay helium further exacerbates the material degradation by significantly reduce the fracture toughness. Because the material inventory is limited and the specimen preparation time is long in machining, pre-cracking, and charging with hydrogen (and with additional time to allow for aging if hydrogen isotopes are used), it is imperative to develop an effective predictive numerical method to reduce testing.

In this preliminary work, computational techniques have been developed to simulate fracture toughness tests and have been demonstrated for hydrogen-charged conventionally forged (CF) 21-6-9 austenitic stainless steel. The uniaxial tension test data are used to determine a stress-strain relation for finite element analyses. Due to the small effects of the hydrogen

concentration, the tensile true stress-true plastic strain curve of the hydrogen-charged CF 21-6-9 stainless steel are estimated to be very close to the uncharged one.

Standardized arc-shaped specimens of the uncharged and the hydrogen-charged CF 21-6-9 steels were tested for fracture resistance (J-R) curves. Finite element models are constructed with cohesive elements to simulate crack extensions. The PPR user-defined cohesive element subroutine [11,12] is adopted but with an exponential traction-separation law in this study. The cohesive strength σ_{max} is estimated by fitting the maximum load of the load vs. displacement test data for the arc-shaped specimens of the hydrogen-charged steel, and the cohesive energy Γ is selected as the J-integral at the maximum load from the experimental J-R curve for the arc-shaped specimen. This approach is shown to be successful in predicting the relationships between the load, displacement, and crack extension. However, the correlation between the load and crack extension curves will need further research to improve the predictive capability. Future research will focus on correlating the cohesive parameters such as the cohesive strength σ_{max} and the cohesive energy Γ to the microstructural features, and to develop an effective modeling strategy for predicting the fracture resistance curves to account for the decay helium in steels.

REFERENCES

[1] Morgan, M.J., 1991, "The Effects of Hydrogen Isotopes and Helium on the Flow and Fracture Properties of 21-6-9 Stainless Steel," Proceedings of the Morris E. Fine Symposium, TMS, Warrendale, PA, pp. 105-111.

[2] Morgan, M.J., 2008, "Tritium Aging Effects on the Fracture Toughness Properties of Forged Stainless Steel," in Materials Innovations in an Emerging Hydrogen Economy, John Wiley & Sons, Inc. pp. 221-235.

[3] Tvergaard, V. and Hutchinson, J.W., 1992, "The Relation between Crack Growth Resistance and Fracture Process Parameters in Elastic-Plastic Solids," Journal of the Mechanics and Physics of Solids, 40(6), pp.1377-1397.

[4] Tvergaard, V. and Hutchinson, J.W., 1996, "Effect of Strain-Dependent Cohesive Zone Model on Predictions of Crack Growth Resistance," International Journal of Solids and Structures, 33(20–22), pp. 3297–3308.

[5] Siegmund, T. and Brocks, W., 2000, "A Numerical Study on the Correlation between the Work of Separation and the Dissipation Rate in Ductile Fracture," Engineering Fracture Mechanics, 67(2), pp.139-154.

[6] Roychowdhury, S., Arun Roy, Y. and Dodds, R.H., 2002, "Ductile Tearing in Thin Aluminum Panels: Experiments and Analyses Using Large-Displacement, 3-D Surface Cohesive Elements," Engineering Fracture Mechanics, 69(8), pp. 983–1002.

[7] Cornec, A., Scheider, I. and Schwalbe, K.H., 2003, "On the Practical Application of the Cohesive Model," Engineering Fracture Mechanics, 70(14), pp.1963-1987.

[8] Wu, S., Sung, S.-J., Pan, J., Lam, P.-S. and Scarth, D.A., 2017, "Crack Extensions in Compact Tension Specimens of Hydrided Irradiated Zr-2.5Nb Materials Using Cohesive Zone Model," Paper Number PVP2017-65022, Proceedings of the ASME 2017 Pressure Vessels & Piping Conference, Waikoloa, HI, USA, American Society of Mechanical Engineers, New York, NY.

[9] ASTM E647-95a, "Standard Test Method for Measurement of Fatigue Crack Growth Rates," 1999 Annual Book of ASTM Standard Volume 3.01 Metals-Mechanical Testing; Elevated and Low-Temperature Tests; Metallography, American Society for Testing and Materials, 1999.

[10] ASTM E1820-99, "Standard Test Method for Measurement of Fracture Toughness," 1999 Annual Book of ASTM Standard Volume 3.01 Metals-Mechanical Testing; Elevated and Low-Temperature Tests; Metallography, American Society for Testing and Materials, 1999.

[11] Park, K., Paulino, G.H., and Roesler, J.R., 2009, "A Unified Potential-Based Cohesive Model of Mixed-Mode Fracture," Journal of the Mechanics and Physics of Solids, 57, pp. 891–908.

[12] Park, K. and Paulino, G.H., 2012, "Computational Implementation of the PPR Potential-Based Cohesive Model in ABAQUS: Educational Perspective," Engineering Fracture Mechanics, 93, pp. 239-262.